

Design of a High Efficiency Compact Centrifugal Compressor for Rotorcraft Applications

E.A. Lurie, P.R. Van Slooten, G. Medic, J.M. Mulugeta, B.M. Holley, J. Feng, O. Sharma

United Technologies Research Center

East Hartford, CT

Elizabeth.Lurie@pw.utc.com

R. Ni

AeroDynamic Solutions, Inc.

Current and envisaged future airport congestion levels motivate the need for increased use of high-performance rotorcraft and rotary wing aircraft. The turboshaft engines that power these aircraft must have high power density, fuel efficiency, and wide operability. The lower physical flows associated with turboshaft engines for rotorcraft, and the high overall pressure ratios (OPRs) required for performance, motivate the use of centrifugal compressors as the last stage of compression. This paper describes the design of a high efficiency, compact centrifugal stage scaled for use as a measurement test bed that is representative of a state of the art compressor stage in rotorcraft engines. In addition to the design activity, this paper outlines the development of the rig instrumentation layout through inspection of CFD results. The instrumentation layout contains high density static and dynamic pressure measurements, to be used for validating design and analysis tools, and for acquiring physics insight to enhance centrifugal compressor design and performance capability. The fabrication of this stage is underway for initial test entry in 2011.

INTRODUCTION

Centrifugal compressors have been extensively used in a variety of products over the last century and in rotorcraft engines over the last 60 years. These devices provide reliable compression in very compact configurations. Extensive databases, design rules, and criteria are available in most of the design and manufacturing organizations to allow development of these machines. These design processes are highly empirical, utilizing scaling strategies, and rely on prototype testing to achieve design goals. This design process reflects the fact that the flow in these machines is highly complex and dominated by three-dimensional, viscous, and unsteady mechanisms, and results in conservative designs to limit engine program risks. Managing this complex flowfield is a primary limitation to high efficiency designs. Over the past decade, CFD-based tools have begun to be utilized to assess configurations during the detailed design phase. To date these tools have been validated largely by utilizing system level performance metrics. There is a need to validate these tools by utilizing data that elucidates physics of loss generation mechanisms in these machines, to ensure these tools can be used to define the details of the loss reduction concepts with added confidence.

A second limitation to high efficiency centrifugal compressor designs is that the close spacing of the rotating impeller and stationary diffuser rows can cause performance and durability issues. Matching a vane diffuser to an impeller is a nontrivial task due to the complicated flow mechanics involved and the absence of

quantitative understanding. Satisfactory performance of an individual component does not guarantee that the combined stage design will also have satisfactory efficiency and flow range. Considerable resources can be spent during an engine development program to rework components that are found only during the rig test phase, not to be well matched. For durability concerns, the unsteady interaction of the impeller-diffuser pair can cause large unsteady blade loads on each, and can be an excitation source for high cycle fatigue. Although there are a number of publications describing impeller-diffuser interaction [for example, 1, 2, 3], no clear guidelines exist on optimizing performance by controlling impeller-diffuser gap, diffuser vane solidity, or vane throat area. Because the interaction losses are inherently unsteady, CFD-based design processes must include unsteady analyses to assess its impact on overall performance.

The purpose of this effort is to identify key technical barriers to advancing the state-of-the-art of small centrifugal compressor stages; to delineate the measurements required to provide insight into the flow physics of the technical barriers; to design, fabricate, install, and test a state-of-the-art research compressor that is representative of the rear stage of an axi-centrifugal aero-engine; and to acquire detailed aerodynamic performance and research quality data to clarify flow physics and to establish detailed data sets for future application. The design activity centered on the replacement of the NASA CC3, a well studied compressor that was tested over many years at the Small Engine Components Test Facility at NASA Glenn Research Center [4, 5, 6]. To fit within the existing test facility and to facilitate component re-use, certain key design parameters were fixed, including impeller tip diameter, impeller rotational speed, and impeller inlet hub and shroud radii. The design target was

to raise total pressure ratio while also increasing efficiency and reducing the maximum diameter of the stage. This paper describes the design effort of the “HECC” High Efficiency Centrifugal Compressor stage and delineation of measurements; fabrication of the compressor is underway and testing is expected to begin in mid-2011.

DESIGN REQUIREMENTS

The intent of the design effort is to develop a centrifugal stage that is representative of the final stage of an axi-centrifugal compressor for rotorcraft applications. To that end, the performance requirements at engine scale and at rig scale are shown in Table 1. Also included are values for the existing CC3 rig. The rig is geometrically scaled twice as large, approximately, as the engine scale, making it easier to accommodate dense levels of instrumentation. The geometric scale factor varies as [7]:

$$\frac{L_{engine}}{L_{rig}} = \sqrt{\frac{\dot{m}_{engine}}{\dot{m}_{rig}}} \quad (1)$$

The engine-scale compressor exit temperature of 950-1000°F corresponds to an overall pressure ratio of 25-30, which is typical of current turboshaft engines. Also, for a multistage turboshaft engine, the mechanical layout would typically drive the impeller geometry to have impeller inlet hub to shroud radius ratio R_{IH}/R_{IS} of about 0.6-0.7 and impeller inlet shroud to tip diameter ratio R_{IS}/R_2 of about 0.6. When scaling to the rig environment, these radius ratios should be maintained. In order to minimize changes to the existing rig hardware, however, this requirement was relaxed and the original ratios were held, at nominally 0.4 and 0.5, respectively. The effect of not holding inlet radius ratios on performance will be addressed in the section on scaling from rig to engine.

DESIGN STRATEGY

In order to achieve the design goals, a design strategy that centered on improvements to the existing rig compressor was implemented. The CC3, shown in Figure 1, was originally design by Allison Engine Company as a high efficiency (peak total-total adiabatic efficiency of 85%), 1.66 kg/s compressor with a total pressure ratio of about 4. It was subsequently scaled to 4.54 kg/s (10 lbm/s) to provide a test article suitable for detailed diagnostics. The CC3 stage consists of an impeller with 15 main and 15 splitter blades with blunt, constant radius trailing edges, and a 24-bladed wedge diffuser that exits into an annular radial-to-axial bend. The impeller blades have constant backsweep angle of 50 degrees from radial. The impeller

Table 1. Design Requirements.

Metric	Engine	Rig	CC3 (Existing rig)
Stage Pressure Ratio	4.0 - 5.0	4.0 - 5.0	4
Exit Corrected Flow (lbm/s)	0.7 - 0.8	2.6 - 3.1	3.1
Work Factor ($\Delta H_0/U_2^2$)	0.6 - 0.75	0.6 - 0.7	0.6
Polytropic Efficiency (TT)	$\geq 88\%$	$\geq 88\%$	86%
Compressor Exit Temp (°F)	950-1000	350-410	425
D_{max}/D_2	≤ 1.45	1.45	1.87
Stability Margin	13%	13%	13%
Geometric Similitude			
Tip Clearance (mil)	6.6	12	12
Fillets (mil)	27/82	50/150	50/150
Surface Finish (mil)	.03	.06	.06
Engine Relevance			
Exit Mach Number	0.15	0.15	0.15
Exit Swirl Angle (deg)	15	15	60
Inlet Radius Ratio (R_{IH}/R_{IS})	0.6	0.38	0.39
Shroud Radius Ratio (R_{IS}/R_2)	0.6	0.5	0.49



Figure 1. Photograph of NASA CC3 reference compressor.

running tip clearance was measured to be 0.1524 mm (0.006 inch) near the leading edge, 0.61 mm (0.024 inch) near mid-chord, and 0.203 mm (0.008 inch) near the exit. The diffuser leading edge is located at radius ratio (diffuser leading edge to impeller trailing edge) $R_3/R_2=1.078$ and exits at diffuser trailing edge to impeller trailing edge radius ratio $R_5/R_2=1.68$. The overall diameter of the stage is $D_{max}/D_2=1.87$.

As an initial assessment of CFD predictive capability, comparisons were made to the existing data for the baseline CC3, which was tested in both vaneless diffuser and stage configurations [5]. The commercial solver Code LEO with rapid grid generation Code WAND, provided by

AeroDynamic Solutions, Inc., was selected as a CFD tool. The structured grid is an OHHHH topology with first grid point from the wall located to capture near-wall effects, with distance to the first grid point from the wall set such that the viscous wall distance (y^+) is near 1. Code LEO is a density-based finite volume CFD code [8] that provides numerical solutions on either a multi-block structured mesh or an unstructured mesh; for the present study, structured meshes were used. Code LEO also uses either a multi-grid scheme or a residual propagation scheme for convergence acceleration. Wilcox's 1998 k- ω turbulence model [9] is implemented in Code LEO. For the present study, the wall integration option is used to determine flow properties near solid surfaces. Grid sensitivity studies had previously been performed by AeroDynamic Solutions for the CC3 configuration; for cases reported here, a grid count of about 1M was utilized. All steady-state CFD models of stage configurations used a mixing plane interface between impeller and diffuser rows. Unsteady time-accurate CFD analyses use a sliding interface between impeller and diffuser rows. Assumed inlet conditions for all simulations include standard day conditions, 1% turbulence intensity and zero inlet swirl. Solid surfaces are treated as adiabatic. The working fluid is air with constant specific heat of $\gamma=1.395$. The predicted results are compared to data in Figure 2 and Figure 3. For the impeller with vaneless

diffuser, Figure 2, the overall trends of the CFD predictions are well compared to the rig data, considering that the CFD model uses the same running tip clearance for all operating speeds. At 100% design speed and corrected flow rate of 10 lbm/sec, steady-state CFD overpredicts total-to-total efficiency by 0.9% and the choke mass flow by less than 1%. For the stage, Figure 3, at 100% design speed and corrected flow rate of 10 lbm/sec, steady-state CFD tends to overpredict total pressure ratio by 3%, temperature ratio by 0.3% (not shown), total-to-total adiabatic efficiency by 0.4%, and choke mass flow by 4%. Unsteady simulations of a 120° sector, consisting of 5 impeller main/splitter blade pairs and 8 diffuser vanes, used a sliding interface and 3000 time steps per revolution (equivalently, 100 time steps per trailing edge pitch). Simulations were run for 2 to 4 revolutions for cyclic convergence. Results of the unsteady simulation compared to data are shown in Figure 3, where it is seen that the predicted efficiency near design point and stall is closer to the measured data, but the choke flow is still overpredicted.

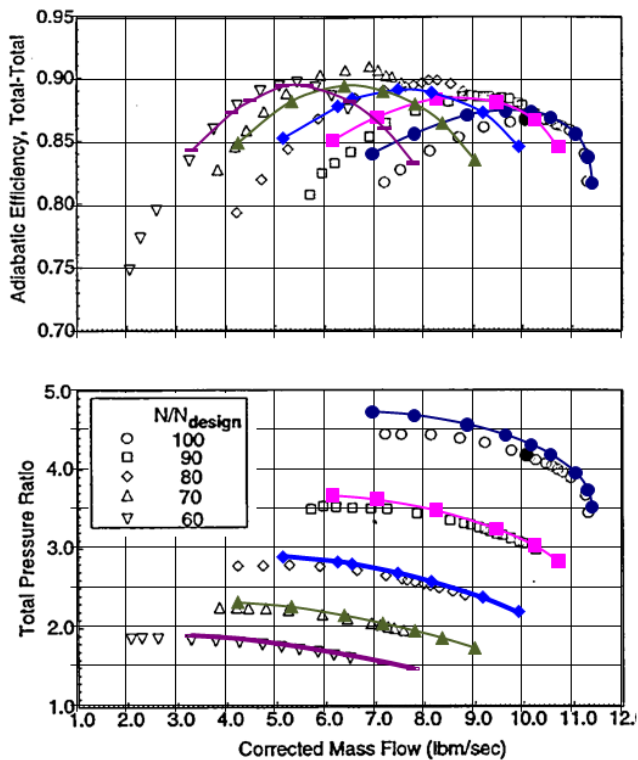


Figure 2. Performance map of CC3 impeller with vaneless diffuser, measurements (open symbols) vs. steady-state CFD results (closed symbols).

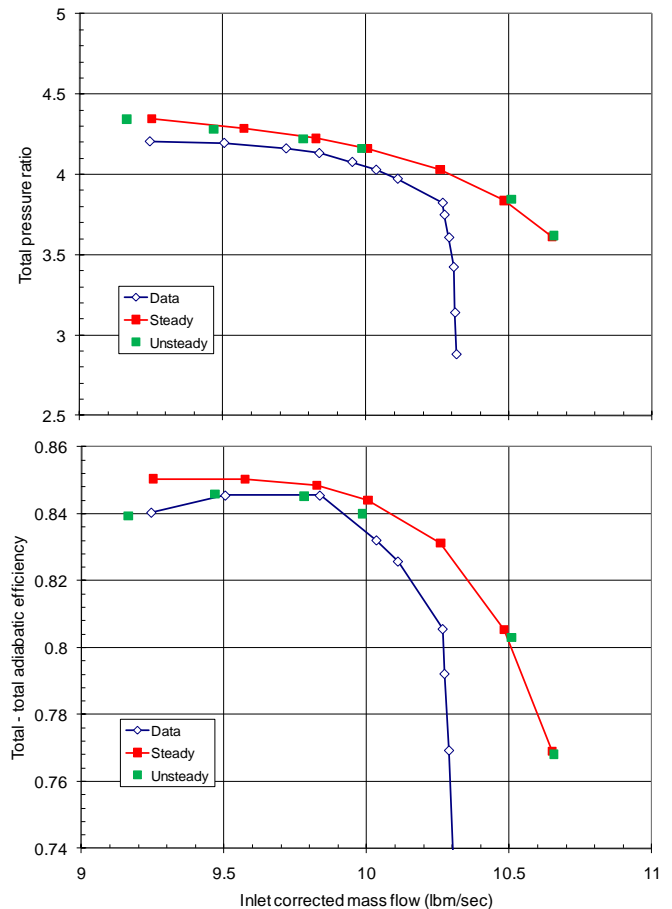


Figure 3. 100% design speed compressor map for CC3 stage, measurements (open symbols) vs. CFD steady-state (red) and unsteady (green) results.

Following the initial calculations, more detailed inspection of the calculated flowfield was done in order to illustrate dominant flow physics. Figure 4 shows contours of entropy generation at different locations through the impeller, at the design operating condition. Dominant losses develop in the impeller exducer passage and collect along the shroud. Circumferentially averaged exit profiles for the vaneless diffuser configuration, shown in Figure 5, indicate that the flow is relatively weak at the shroud side, as evidenced by the near-zero radial velocity, in general agreement with measurements [6]. Velocity vectors in the diffuser passage, in the vicinity of the hub, for the stage calculation, Figure 6, show evidence of separation on the diffuser pressure side.

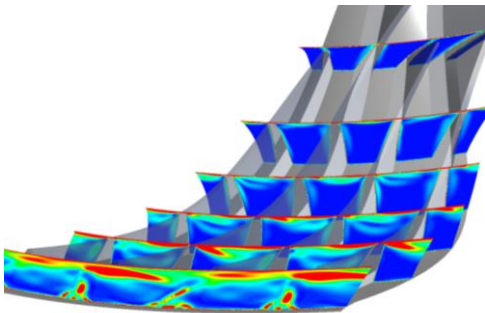


Figure 4. Contours of entropy generation at design condition, CC3 impeller.

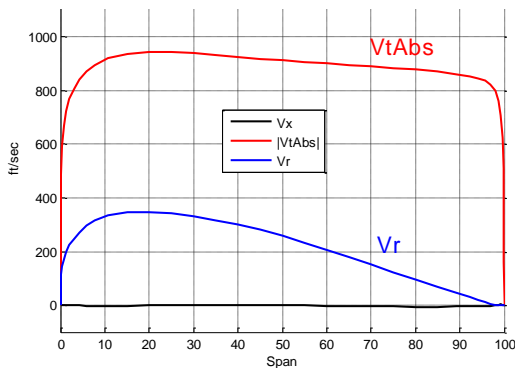


Figure 5. CC3 impeller, circumferentially averaged velocity profiles at radial location $1.18 \times$ impeller tip radius, about 2.5 blade widths downstream of the trailing edge.

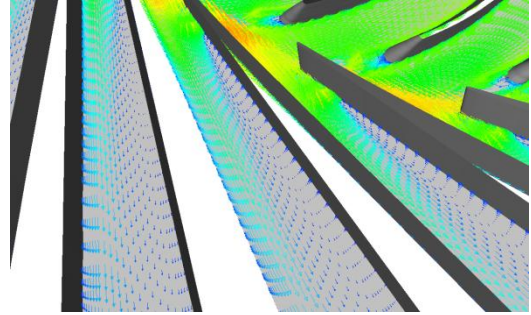


Figure 6. Velocity vectors in the CC3 diffuser passage at design condition.

In order to address the weak shroud side flow, a wide ranging sensitivity analyses was performed. Three-dimensional aerodynamic concepts that have found success in axial turbomachinery components were applied to the CC3 geometry in order to identify opportunities for improvement. Concepts assessed included impeller blade lean, impeller blade bow, impeller leading edge shape, impeller trailing edge shape, diffuser vane sweep, diffuser vane lean, diffuser vane leading edge shape, and diffuser endwall contouring. Examples of the modified impeller geometries are shown in Figure 7 and of the modified diffuser geometries are shown in Figure 8.

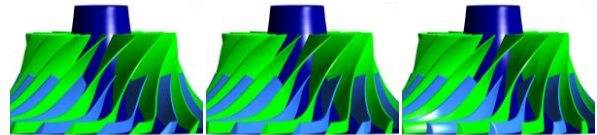


Figure 7. Left to right: Baseline CC3 impeller, CC3 impeller with lean applied, CC3 impeller with bow applied.

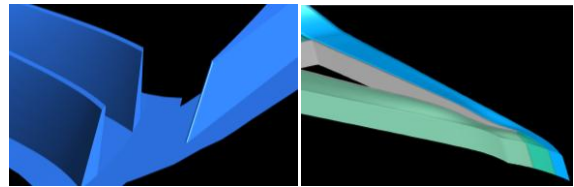


Figure 8. Left: Example of diffuser with leading edge sweep. Right: Example of endwall contouring applied to diffuser hub endwall after CFD-based optimization.

Impeller trailing edge shaping was found to have a strong effect on loading, efficiency, and exit profiles, in addition to maximum capacity. This was found by replacing the existing constant radius trailing edge with a rounded trailing edge, while maintaining the same maximum radius, during the grid generation process. The modified impeller, when combined with a vaneless diffuser,

was found to have noticeably higher total pressure ratio and efficiency, as seen in Figure 9. Also, the circumferentially averaged exit profiles for the impeller with rounded trailing edge were found to have less evidence of separation, Figure 10. The reason for the significant increase in pressure rise is specific to the way in which the trailing edge was rounded and can be explained by referring to Figure 11. In this instance, when moving from constant radius to rounded trailing edge, material is preferentially removed from the suction side of the blade while the pressure side remains largely unchanged. This results in less blade lean and also reduces the backsweep angle; reduced backsweep angle can be shown via the Euler work equation to raise the pressure rise through the impeller [7]. Also, the presence of more uniform exit velocity profiles is an indication that secondary flows have been reduced through the impeller passage.

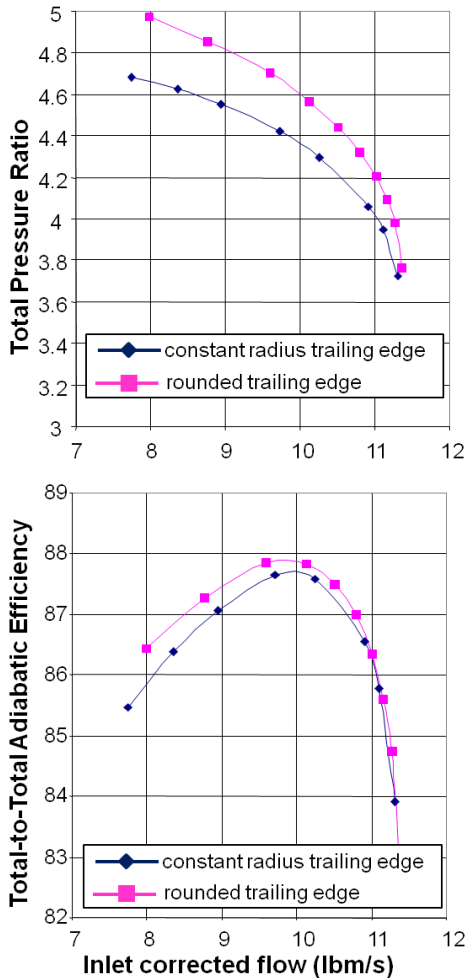


Figure 9. CFD predicted performance map of CC3 impeller with constant radius trailing edge vs. rounded trailing edge.

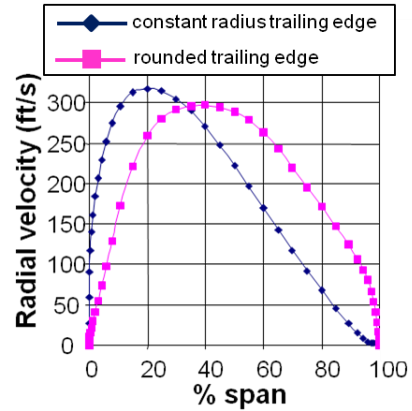


Figure 10. CFD predicted radial velocity at impeller exit ($R/R_2=1.20$) for impeller and vaneless diffuser. Operating condition is 10 lbm/s inlet corrected flow.

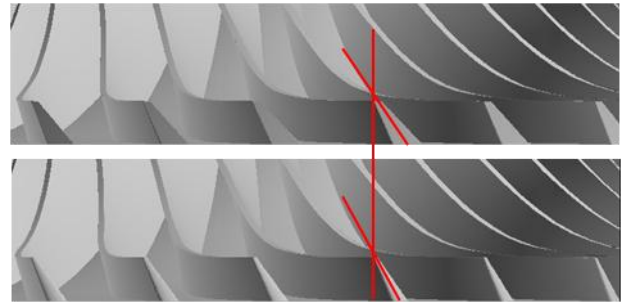


Figure 11. Top: CC3 impeller with constant radius trailing edge. Bottom: CC3 impeller with rounded trailing edge.

Given the results of the scoping studies, then, the design strategy was to target uniform impeller exit profiles, via backsweep distributions, impeller blade shaping, and flowpath shaping, in order to provide uniform entry profiles to the two-dimensional diffuser blades, and as an indicator of reduced secondary flows. Concurrently, the overall performance goal was to increase pressure ratio (via backsweep reduction) and efficiency while maintaining stall margin. This strategy, if executed successfully, can decrease specific fuel consumption by increasing stage pressure ratio or by decreasing the required number of axial stages.

Impeller Design

Meanline sensitivity studies were performed to assess the impact of changes in principal blade dimensions on pressure ratio, efficiency, and choke mass flow rate, assuming a fixed impeller diameter and operating speed. The meanline slip factor was calibrated to the CC3 rig data, Figure 12. Examples of meanline study output is shown in Figure 13 and Figure 14. Meanline analyses were exercised in order to select the impeller blade exit width and diffuser throat area.

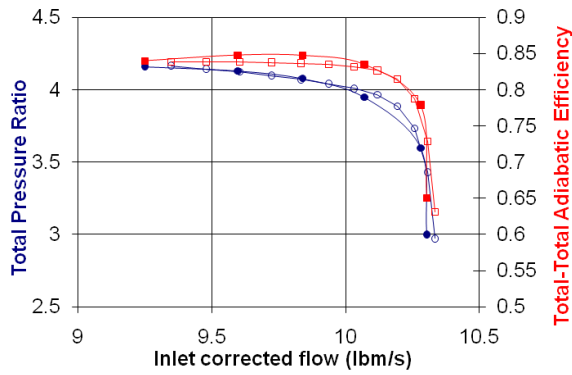


Figure 12. Results of calibration of meanline to CC3 data, prior to geometry sensitivity studies.

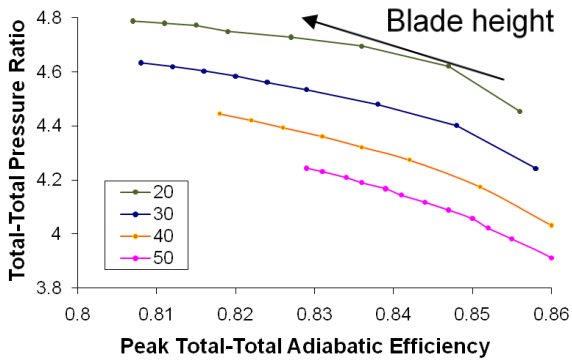


Figure 13. Meanline study prediction of peak pressure ratio and efficiency for varying exit blade height and impeller backsweep angle.

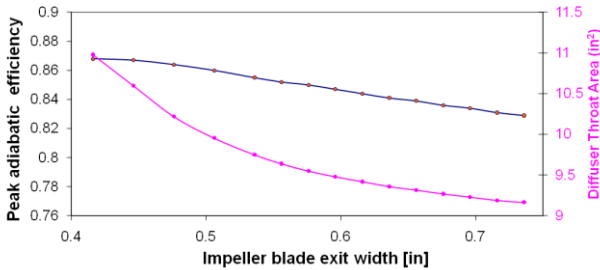


Figure 14. Meanline study prediction of peak efficiency and diffuser throat area for varying impeller blade exit width, for fixed impeller backsweep angle.

Following the meanline study, detailed impeller blade design began in earnest. A parent impeller with backsweep varying from 22-30 deg from hub to shroud was selected for study. Progressively higher backsweep from hub to shroud removes excessively high loads from outer portions of the blade. A series of local blade shape modifications was performed, and the impact of each on overall performance, blade loading, and impeller exit profiles was

assessed using CFD. Each impeller was paired with the same vaneless diffuser; the meridional flowpath can be seen in Figure 15. The compressor map results of the study are shown in Figure 16. In this instance, modification of the trailing edge has the largest impact, causing a decrease in pressure ratio and an increase of efficiency of 0.4%. In this instance, opposite to the effect seen on the CC3 impeller, rounding the trailing edge reduces the pressure ratio. The blade metal angle is more radial to begin with, and so the effect of rounding is more evenly distributed to pressure and suction side with no change to lean, Figure 17.

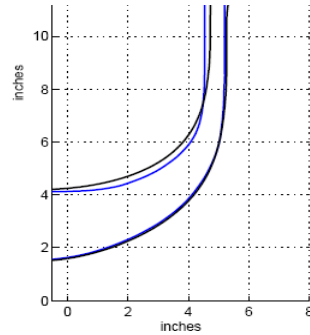


Figure 15. Comparison of flowpath for CC3 (blue) and HECC impeller design studies (black).

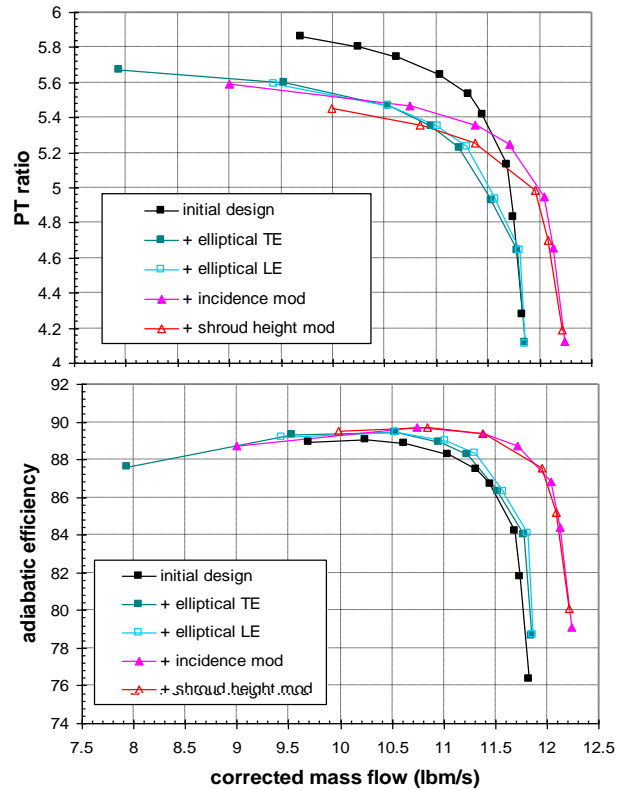


Figure 16. CFD prediction, 100% design speed compressor map for parent 20 deg backsweep impeller (initial design), followed by sequential additions of modifications.

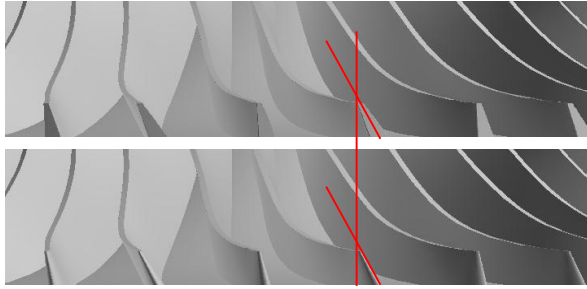


Figure 17. Top: Parent 20 deg backsweep impeller with constant radius trailing edge. Bottom: Parent 20 deg backsweep impeller with rounded trailing edge.

The best of these nominal 20 deg backsweep designs was confirmed to have achieved target two-dimensional exit flowfields, Figure 18. The exit radial velocity is more uniform, especially at the shroud side (span=100%). This leads to lower shroud-side endwall losses.

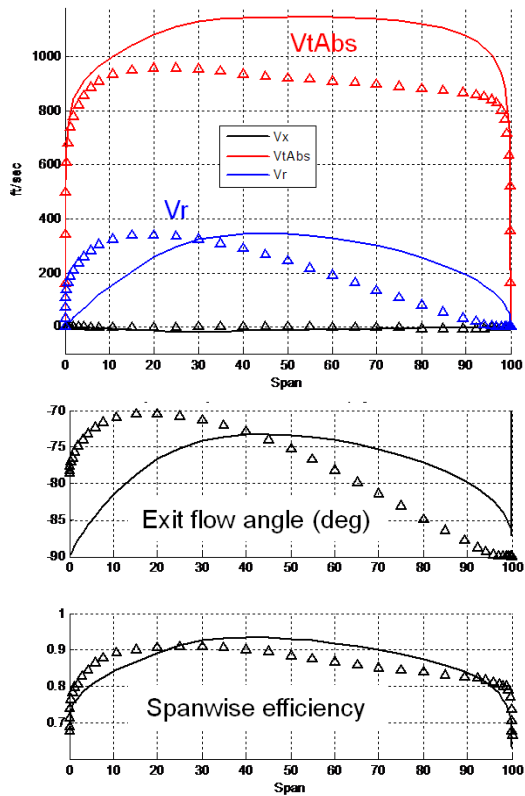


Figure 18. Impeller blade exit circumferentially averaged profiles. Open symbols: CC3. Solid line: Parent 20 deg backsweep impeller design.

The parent impeller and its derivatives all are predicted to have excess pressure ratio capability, suggesting that the backsweep could be increased to lower pressure ratio and increase stability margin [7]. This trade of pressure ratio vs. stability margin is also more consistent

with product demand. The best of the 20 deg backsweep configurations was then modified by increasing the backsweep to spanwise varying 32-42 deg, and through CFD was confirmed to maintain the 2D exit profiles. A comparison of the surface pressure at different spanwise stations is shown as isentropic Mach number vs. normalized chord length in Figure 19, where it is seen that the new design shifts loading aft, and that the flow is accelerating over the last part of the blade, which reduces the likelihood of separation so often found in the exducer area. Also, the

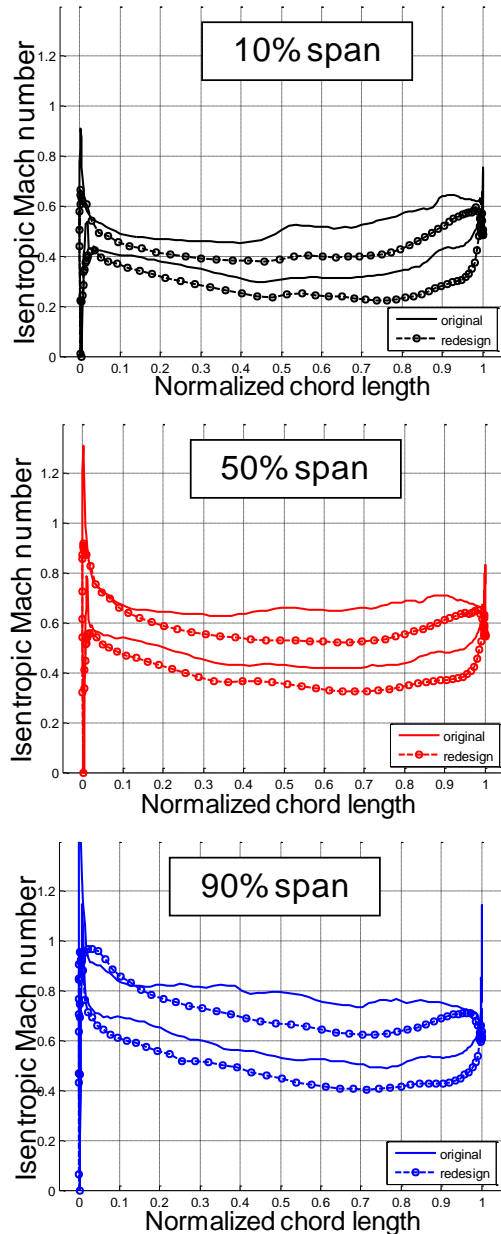


Figure 19. Isentropic Mach number vs. normalized chord length at varying spanwise locations for original CC3 (solid) and redesigned HECC impeller (symbols).

blade loading, defined as the difference between the pressure side and suction side surface pressure, normalized on the dynamic pressure based on tip speed, is shown in Figure 20. The redesigned impeller achieves higher loading at both leading edge and trailing edge regions.

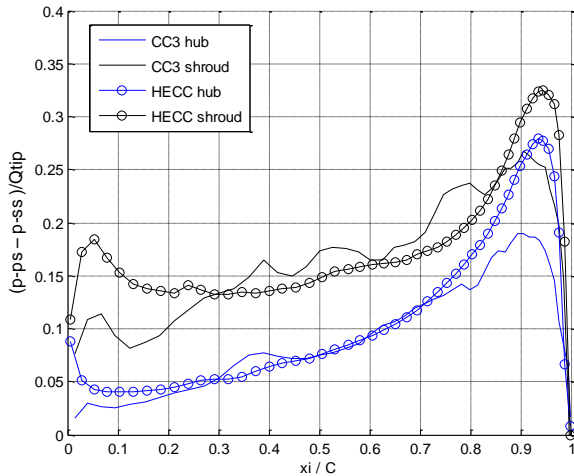


Figure 20. Blade pressure loading for original CC3 (solid) and redesigned HECC impeller (symbols), for the same total pressure ratio.

Diffuser Design

In order to reduce the maximum diameter of the compressor while increasing overall total-to-static efficiency, alternative topologies to the wedge diffuser were considered. A view of the target flowpath is shown in Figure 21; the reduction of maximum diameter lowers the available lossless pressure recovery by about 30%. Careful tailoring of the diffuser geometry is needed to maximize pressure recovery. As a first step, alternative topologies at the same maximum diameter as the original CC3 were considered in order to identify the highest recovery layout, Figure 22. Vane diffusers with splitters were found to maintain total-to-static efficiency with 5% increased pressure recovery, and were selected to be considered for the final reduced diameter design. In order to balance the pressure recovery through both side of the splitter passage, the splitter was positioned off the midpassage centerline and at a slight stagger angle, to match each side’s length to width and area ratios, by reference to classic diffuser maps [11]. By shifting the splitter in this manner, an additional +0.3% total-to-static efficiency is gained over the midpassage splitter placement. Also, compared to the original surface pressure distributions, the shifted splitter configuration creates more balanced loading between the two elements for radius $R > 10.5$ inches, Figure 23.

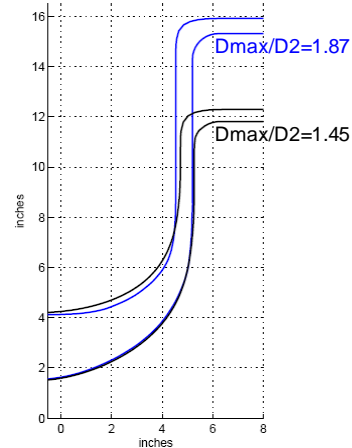


Figure 21. Original (blue) and redesigned (black) flowpaths, showing 23% reduction in stage maximum diameter. Reducing the exit diameter limits the amount of diffusion available.

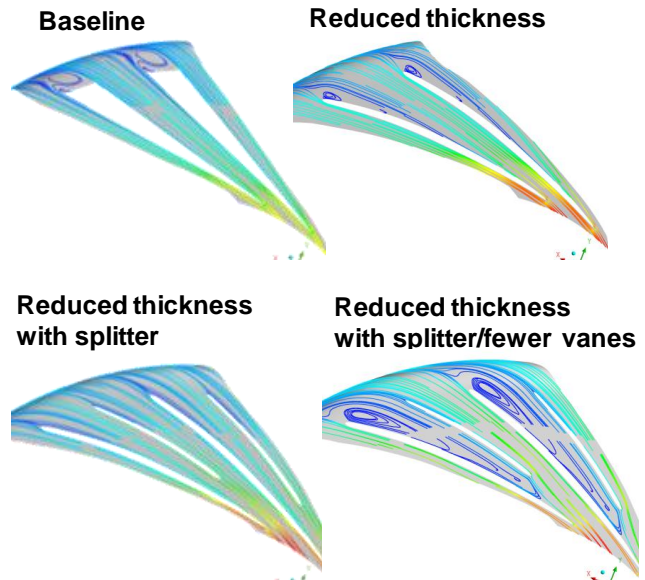


Figure 22. Examples of topologies considered at same maximum diameter as original CC3. Streamlines at 50% span shown, indicating that the configuration “Reduced thickness with splitter/fewer vanes” is not favorable.

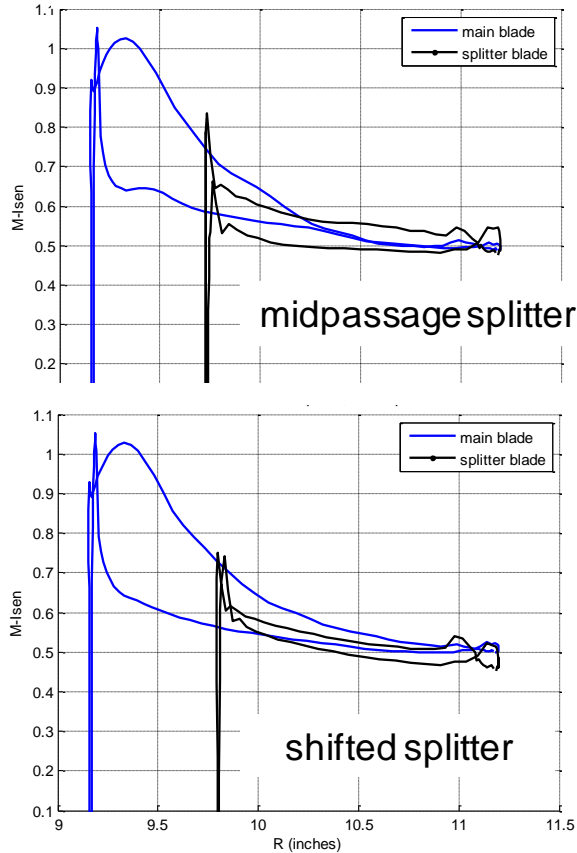


Figure 23. Comparison of loading distributions for vane diffuser with splitter, for splitter placed identically in midpassage (top) or shifted in order to balance pressure recovery on both sides (bottom).

Exit Guide Vane Design

The exit flow from the diffuser still contains a significant amount of swirl velocity, which must be reduced for satisfactory combustor performance in an engine application. To that end, a row of exit guide vanes was designed to target a stage exit Mach number of 0.15 and swirl angle of 15 degrees from axial. The exit guide vanes were developed as an isolated row, using the circumferentially averaged exit profiles from the diffuser row as the inlet boundary condition to the three-dimensional CFD model. A trade study was executed that considered variations in solidity (by varying blade count and axial distance) and stagger angle, for two airfoil sections. The goal is to minimize total pressure loss while meeting the target exit swirl angle. After comparing about 50 permutations, Figure 24, two configurations were downselected for computations of all three components in the stage, using a mixing plane between the rotating impeller and stationary diffuser rows, and point-to-point matching of a single passage of the 20-bladed diffuser with

three passages of a 60-bladed exit guide vane row. In this way, the effect of clocking the exit guide vanes relative to the diffuser blades could be studied; in the optimal configuration, a “free” increase in total-to-static efficiency of 0.1% is found, Figure 25. The difference can be seen by considering the convection of the diffuser wakes through the EGV row at design point, Figure 26; in an engine application, the blade counts of the two stationary rows would be selected such to minimize any periodicity of wake interaction. For the rig, the final clocking angle was selected based on most uniform pressure distribution on each of three blades. Finally, the radial-to-axial bend geometry was optimized in a process that couples the CFD solver Code LEO to mesh morphing software Sculptor (a product of Optimal Solutions Software, LLC) with optimizer iSight (a product of Simulia of Dassault Systèmes), to minimize total pressure loss. In this instance, the CFD model includes a single passage of the impeller, diffuser, and EGV rows; the bend and EGV flowpath are geometry are manipulated using 8 control points on the hub and 8 on the shroud that are allowed to vary radially. The shroud control points are constrained not to exceed the stage maximum diameter. The resulting change in the bend geometry, Figure 27, was found to improve total-to-static adiabatic efficiency by 0.25%.

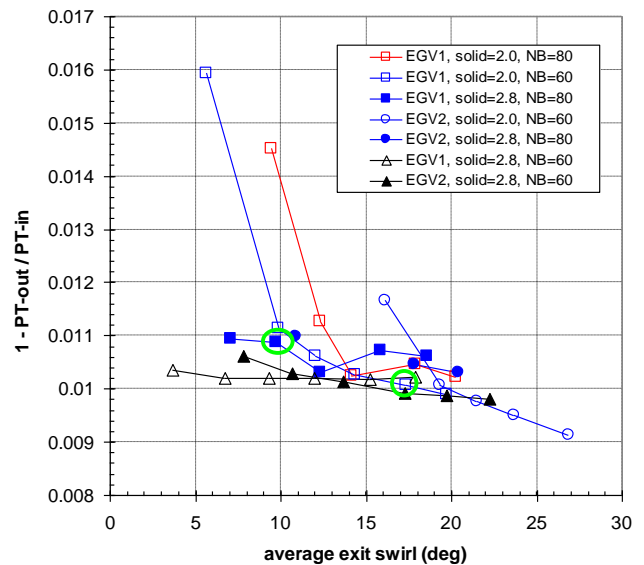


Figure 24. Results of EGV airfoil section trade study, in which camber and solidity were varied for two airfoil sections to find minimum total pressure loss that meets target exit swirl angle. Configurations circled in green were downselected for further analyses via stage calculations.

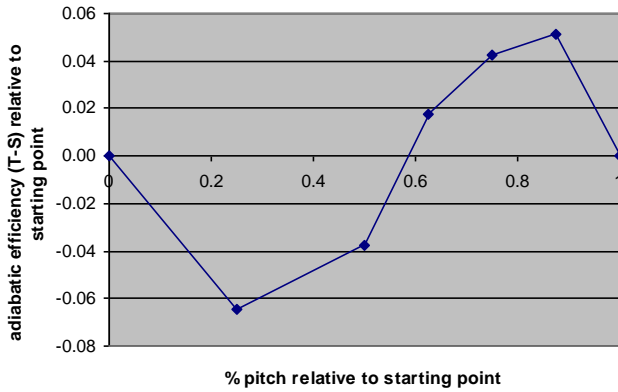


Figure 25. Variation in total-to-static efficiency due to positioning of EGV row relative to diffuser row.

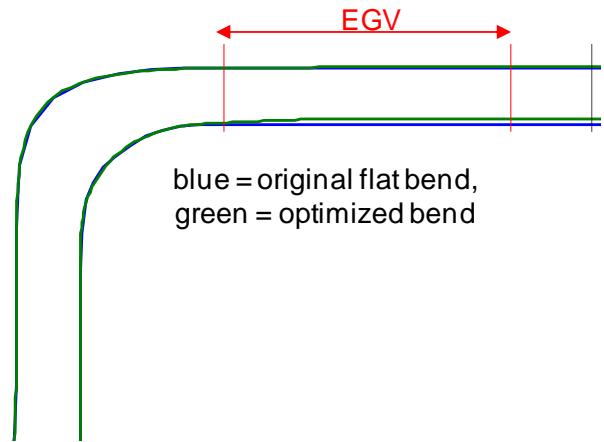
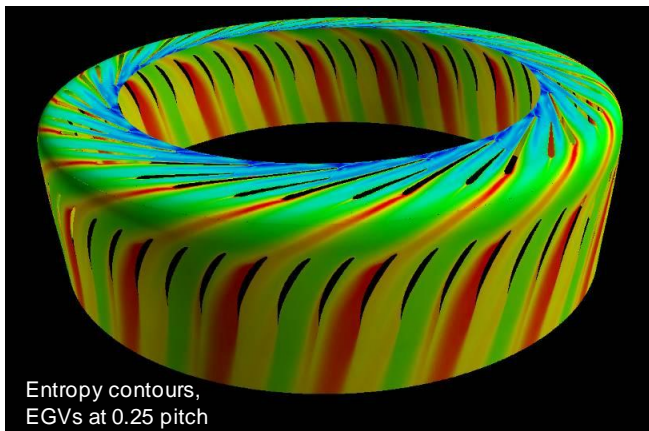
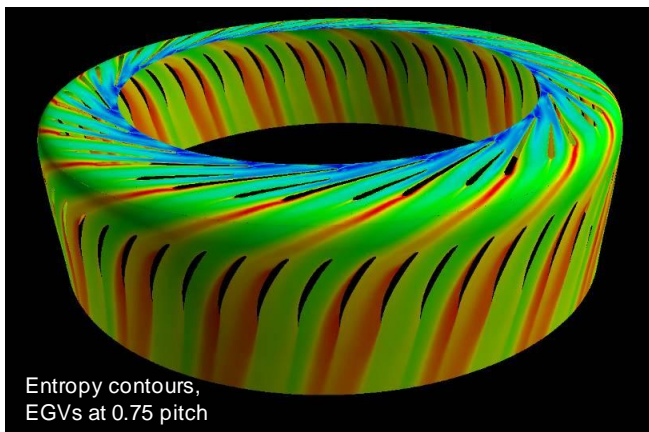


Figure 27. Results of optimization of radial-to-axial bend area, showing original flat bend (blue) and redesigned curved bend (green).



Entropy contours, EGVs at 0.25 pitch



Entropy contours, EGVs at 0.75 pitch

Figure 26. Comparison of entropy contours for least favorable (top) and most favorable (bottom) position of EGV row relative to diffuser row.

The final configuration geometry is given in Table 2. After each individual component was designed, stage calculations were made that assessed the overall performance and to compare the baseline CC3 compressor. Following completion of the impeller and diffuser design, an entire compressor map was generated, using a steady state CFD model with mixing plane assumption between the rotating and stationary row, Figure 28. This map shows contours of total-to-total polytropic efficiency instead of total-to-static, because it does not include the EGV row, and is a more direct comparison with the CC3 (which does not have EGVs) and the anticipated rig data. In this map it is also seen that the preferred inlet corrected mass flow rate of 10 lbm/sec achieves best performance at 95% rpm, with total pressure ratio of 4.4 and total-to-total polytropic efficiency of greater than 89%.

Table 2. Geometric parameters of the redesigned centrifugal compressor stage.

	Value	Hub	Shroud	Units
Impeller Blade Inlet Diameter		3.190	8.479	in
Impeller Splitter Inlet Diameter		5.315	9.474	in
Impeller Exit Diameter		16.988	16.998	in
Impeller Exit Blade Height	0.609			in
Leading edge lean angle	-2			deg
Trailing edge lean angle	-29			deg
Number of Blade/Splitter Pairs	15			-
Tip clearance	0.012			in
Vaned Diffuser Inlet Diameter		18.309	18.309	in
Vaned Diffuser Outlet Diameter		22.398	22.398	in
Vaned Diffuser Channel Height	0.559			in
Number of Vane/Splitter Pairs	20			-
Deswirl Blade Inlet Diameter		23.663	24.594	in
Deswirl Blade Exit Diameter		23.737	24.610	in
Deswirl Vane Axial Chord	2.438			in
Number of Deswirl Vanes	60			-

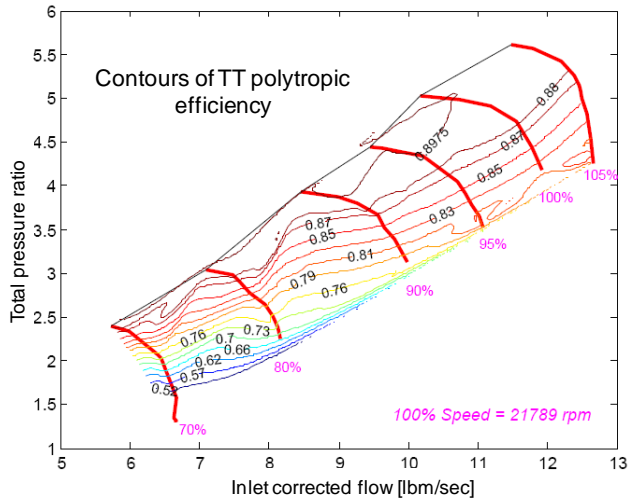


Figure 28. CFD-predicted performance map for redesigned HECC impeller and diffuser stage.

This same configuration was also considered using an unsteady CFD model of a sector of the stage, which includes a 72 deg periodic sector of 3 impeller blade passages and 4 diffuser blade passages. The unsteady calculation was performed to ensure that the predicted performance did not vary substantially from the steady state assumptions when impeller-diffuser interactions were also included. The resulting speedline at 100% design speed is given in Figure 29, in which it is seen that the predicted performance is reduced by approximately 0.5% in the compressor operating area, at no penalty to total pressure ratio. A comparison of the final geometry is given in Figure 30, and of the predicted total-to-static efficiency vs. exit corrected flow in Figure 31.

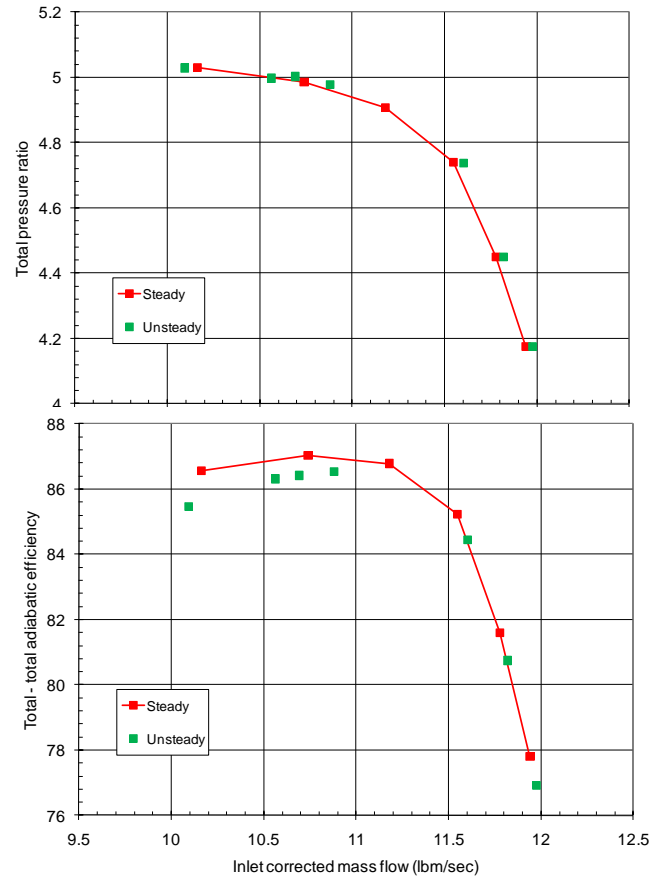


Figure 29. 100% design speed compressor map for redesigned impeller and diffuser, steady-state vs. unsteady CFD models.

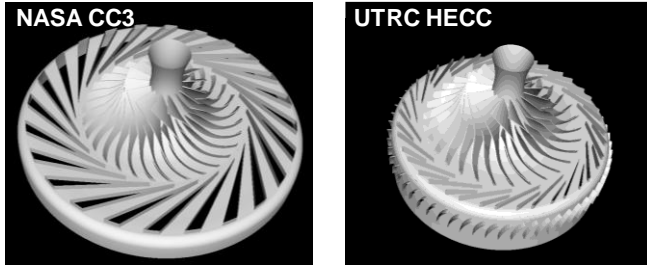


Figure 30. Original (left) and redesigned (right) stage configurations.

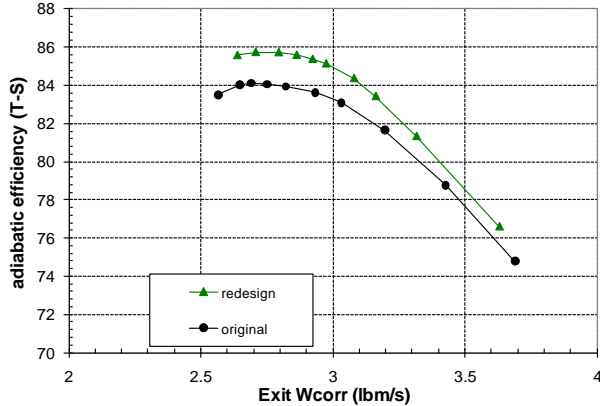


Figure 31. Predicted total-to-static adiabatic efficiency for original CC3 and redesigned stage.

Stage Performance at Rig Scale and Scaling to Engine

In order to project the stage performance to engine scale, three elements are considered: the calibration of CFD to data, the impact of relatively low inlet radius ratio for the rig, and the Reynolds number effect. The geometric scale factor of equation (1) is calculated to be 0.52, assuming the rig operates at 100% design speed and inlet corrected flows of 11 lbm/sec for the rig and 3 lbm/sec for the engine. Other geometric parameters of the rig design are relevant for the smaller engine scale by assuring that once scaled down, the minimum thicknesses and leading and trailing edge radii would conform to standard design and manufacturing practices. The exception to this is in the impeller fillets, the size of which were retained from the original CC3 impeller for direct comparison of the impact of impeller blade shaping on performance.

The performance delta when moving from rig to engine to capture the effect of inlet radius ratio was considered. Larger inlet radii drives higher inlet tip Mach numbers and associated friction and shock losses. The effect was estimated in two ways. First, meanline predictions for the HECC stage with inlet hub-to-inlet shroud ratio increased from $R_{IH}/R_{IS} = 0.37$ to $R_{IH}/R_{IS} = 0.60$, with fixed inlet area and no inlet swirl, were compared, Figure 32, in which it is seen that the higher radii cause an efficiency penalty of 1%.

Second, a survey of recent literature [12] indicates that at similar pressure ratio and work factor to the HECC stage, which has specific speed $N_s=0.6$, and with inlet swirl of 25 deg, as might be found in a multistage aero-engine, the efficiency penalty for increasing radius ratio is about 0.5%, Figure 33.

Finally, the efficiency delta due to Reynolds number effects when scaling from rig to engine is found using the standard formulation [10],

$$\frac{1-\eta_{engine}}{1-\eta_{rig}} = \left(\frac{Re_{rig}}{Re_{engine}} \right)^{0.1} \quad (2)$$

where the Reynolds number is based on inlet flow conditions ρ_1 , μ_1 , the mean inlet absolute velocity V_1 , and the tip diameter D_2 . All of the rig quantities are known from the CFD solutions. The engine conditions are found in the following manner. By assuming an overall pressure ratio, and knowing that portion of the pressure rise through the centrifugal stage, then the portion of pressure rise through the engine's axial stages can be assigned and the inlet pressure to the centrifugal can be known. Based on the design requirements, Table 1, the inlet total temperature is known to be in the range 950-1000°F. The inlet velocity for the engine is found by from the rig inlet Mach number and from the inlet static temperature. Given the range of inlet total temperatures and assumptions of overall pressure ratio in the range 25-30, then, the adiabatic efficiency for the engine is expected to be 0.2-0.7% higher than for the rig. No change in surge margin due to Reynolds number effects is expected since both rig and engine are in the high Reynolds number regime [10].

Given these estimates, the projected aerodynamic performance of the engine version of the HECC stage is estimated in three steps, Figure 34. First, the CFD prediction of efficiency is decremented by the amount overpredicted based on the CC3 data. This decrement captures the effects of additional losses not captured by the steady-state mixing plane model, any rig inlet flow nonuniformity, backplate bleed, fillets, and any other nonideal geometry not present in the CFD model. Second, the range of efficiency penalty due to inlet radius ratio is assessed. Last, the range of increase in efficiency due to Reynolds number effects is added. The net result is a predicted polytropic total-to-total efficiency of 87.9-88.5%.

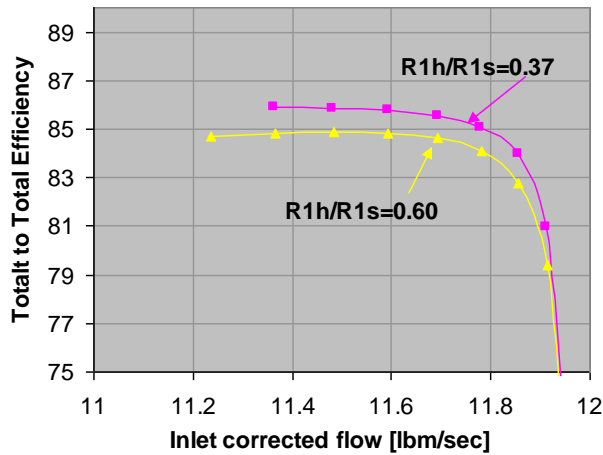


Figure 32. Meanline prediction of total-to-total adiabatic efficiency for varying inlet radius ratio at fixed inlet area, no inlet swirl.

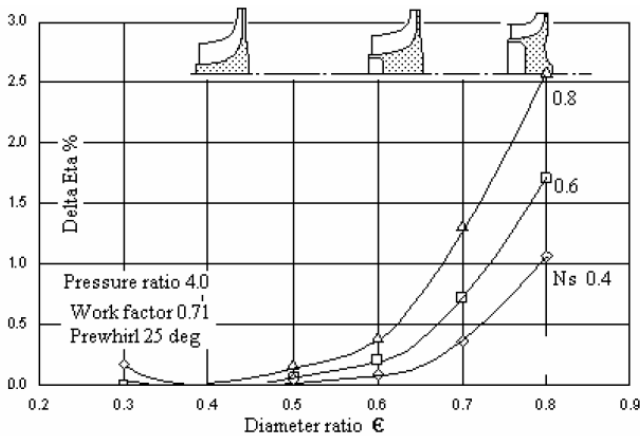


Figure 33. Estimated efficiency reduction vs. diameter ratio $\epsilon = D_{1,rms}/D_2$, at varying specific speeds. HECC stage is specific speed $N_s=0.6$. Reprinted from [12].

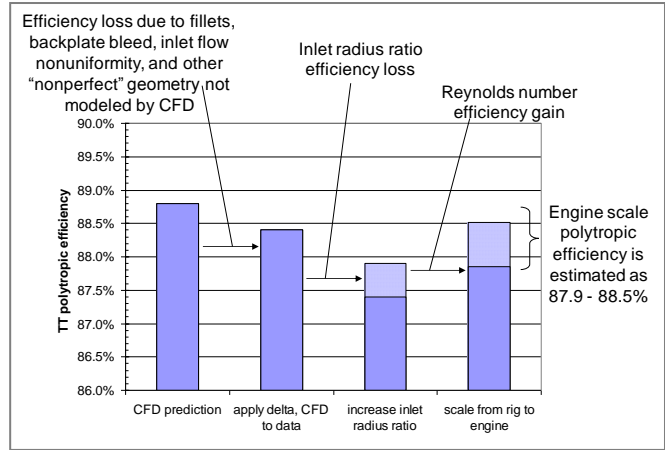


Figure 34. Bookkeeping efficiency deltas from rig to engine scale.

INSTRUMENTATION LAYOUT

The steady-state and unsteady CFD results were interrogated for guidance regarding placement of instrumentation, the purpose of which is threefold: to confirm key improvements of the HECC design; to explore technical barriers; and to provide validation for the design community. In order to assess the overall performance of the stage, twelve exit rating rakes, containing three total pressure and two total temperature measurements each, are located around the exit, clocked circumferentially by diffuser blade pitch and then in 1.5 deg increments, in order to provide flowfield measurements across one entire diffuser blade pitch. Also, there are over 200 static pressure taps throughout the flowpath: along the impeller shroud, in dense fields surrounding one diffuser passage on both hub and shroud side, through the radial-to-axial bend, along three exit guide vanes, and at the stage exit. The selection of tap locations was made based on inspection of the steady-state CFD results for 100% design speed, at choke, peak efficiency, and near-stall conditions, with the goal of providing detailed information in relevant locations. An example of that assessment is shown in Figure 35, in which the CFD prediction of static pressure on the shroud surface surrounding the diffuser main blade is shown, along with the static pressure tap locations.

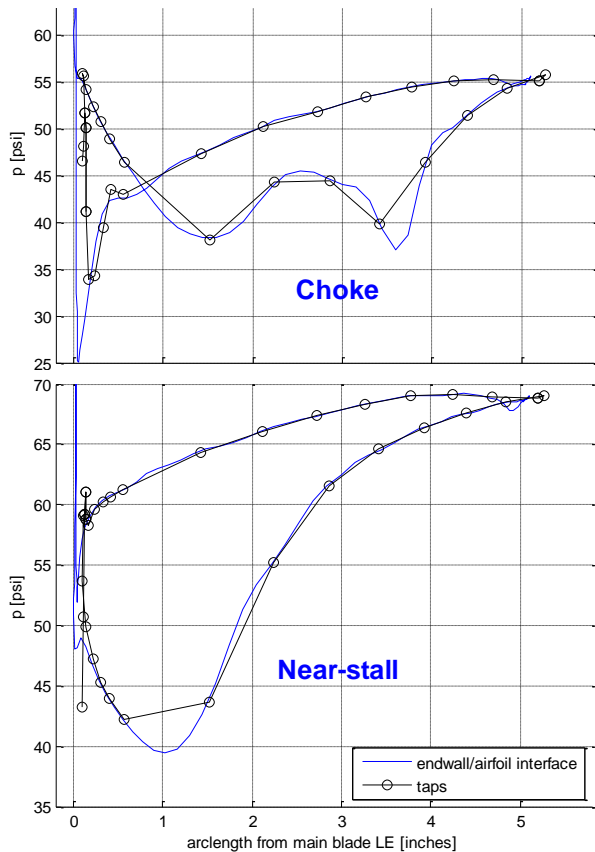


Figure 35. CFD prediction of static pressure near diffuser main blade shroud surface, at choke (top) and near-stall (bottom) conditions. Symbols indicate tap locations.

In order to assess the performance of individual components, provisions for probe access has been created between the impeller and diffuser, and between the diffuser and exit guide vanes. Two diffuser main blades have been fabricated in a modular fashion, allowing for future instrumentation development. The initial configuration has five total pressure measurements along the leading edge, allowing for confirmation of the two-dimensional nature of the impeller exit profiles. Also, one set of three exit guide vanes has total pressure kielheads installed at three spanwise locations per blade.

In order to address technical barriers associated with impeller-diffuser interaction and high cycle fatigue, a set of twenty unsteady pressure transducers were laid out in the region between the impeller trailing edge and through the diffuser passage. Locations were selected based on interrogation of unsteady CFD results at near-stall and choke conditions. A 3x3 array of measurements at (90, 96, 100) percent impeller trailing edge radius in (0, 1/3, 2/3) pitch increments will capture the variation of the pressure field in the stationary frame due to the upstream effect of the diffuser blades. Also, a set of ten measurements through the vaneless space and diffuser passage will capture traveling waves and possible pumping of the pressure field along

either side of the splitter blade. Finally, in order to assess rotating stall, 12 measurements are located at 1.05 times the impeller tip radius, with ten in a pitchwise location that exhibited very small pressure amplitude in the CFD unsteady simulation and two at (1/3, 2/3) pitchwise increments from the other ten. Because the unsteady CFD model only includes four of twenty diffuser passages, it is not expected to capture unsteady phenomena associated with disturbances on the scale of the entire circumference.

The rig also contains provisions for measuring tip clearance via six tip capacitance probes, located at inlet, knee, and exit of the impeller along two arcs separated by 180 degrees. Finally, variable backplate bleed capability is already present in the rig.

CONCLUSIONS

This paper describes the design of a high efficiency, compact centrifugal stage, scaled for use as a measurement test bed that is representative of a state of the art compressor stage in rotorcraft engines. The design activity centered on the replacement of the CC3, a well studied existing compressor. Once in the narrowed-down design space constrained by key blade dimensions, a CFD-based design process that included time accurate calculations of the impeller-diffuser interactions, was used to assess over 50 configurations at over 400 operating points for performance and post-processed flowfield quantities. Enhanced stage efficiency was achieved through careful tailoring of the impeller exit flowfield, such that secondary flow is reduced and two dimensional exit flow is achieved. The final design is predicted to achieve 1.7% higher total-to-static adiabatic efficiency while simultaneously reducing stage maximum diameter by 23%. In addition to the design activity, this paper outlines the development of the rig instrumentation layout, to answer fundamental research and design confirmation questions. The fabrication of this stage is underway for initial test entry in 2011.

ACKNOWLEDGEMENTS

The authors gratefully acknowledge the National Aeronautics and Space Administration for their support under contract NNC08CB03C, as part of management of the Subsonic Rotary Wing vehicle project within the NASA Fundamental Aeronautics Program. Thanks are also extended to Dr. Gerald Welch, Dr. Michael Hathaway, Mr. Edward Braunscheidel, and Mr. Mark Stevens of NASA Glenn Research Center. Finally, authors acknowledge the contributions by Xiangyang Deng and Aamir Shabbir of UTRC and Tony Jones of Hamilton Sundstrand-Power Systems.

REFERENCES

1. Peeters, M., and Sleiman, M., "A Numerical Investigation of the Unsteady Flow in Centrifugal Stages," ASME Paper 2000-GT-0426, International Gas Turbine and Aeroengine Congress and Exhibition, Munich, Germany, May 8–11, 2000.
2. Shum, Y. K. P., Tan, C. S., Cumpsty, N. A., "Impeller-Diffuser Interaction in a Centrifugal Compressor," *Journal of Turbomachinery*, Vol. 122, October 2000.
3. Trebinjac, I., Kulisa, P., Bulot, N., and Rochuon, N., "Effect of Unsteadiness on the Performance of a Transonic Compressor Stage," *Journal of Turbomachinery*, Vol. 131, October 2009.
4. McKain, T.F. and Holbrook, G.J. "Coordinates for a High Performance 4:1 Pressure Ratio Centrifugal Compressor." NASA CR 204134, July 1997.
5. Skoch, G. J., Prahst, P. S., Wernet, M. P., Wood, J. R., Strazisar, A. J. "Laser Anemometer Measurements of the Flow Field in a 4:1 Pressure Ratio Centrifugal Impeller." ASME Paper 97-GT-342, International Gas Turbine and Aeroengine Congress and Exhibition, Orlando, FL, June 2-5, 1997.
6. Larosiliere, L. M., Skoch, G. J., Prahst, P. S., "Aerodynamic Synthesis of a Centrifugal Impeller Using Computational Fluid Dynamics and Measurements," *Journal of Propulsion and Power*, Vol. 15, (9), Sept-Oct 1999.
7. Cumpsty, N.A., *Compressor Aerodynamics*, Krieger Publishing Company, 2004.
8. Ni, R. H., "A Multiple-Grid Scheme for Solving the Euler Equations," *AIAA Journal*, Vol. 20, (11), 1982.
9. Wilcox, D.C., *Turbulence Modeling for CFD*, DCW Industries, Inc., 1993.
10. Japikse, D., *Centrifugal Compressor Design and Performance*, Concepts ETI, Inc., 1996.
11. Runstadler, P.W. and Dolan, F.X., "Diffuser Data Book," Creare Inc. TN 186, May 1975.
12. Rodgers, C., and Brown, D., "High Hub/Tip Centrifugal Compressors," GT2009-59012, Proceedings of ASME Turbo Expo 2009, Orlando, FL, June 8-12, 2009.